Uncertainty Estimates for Sonic-Boom Pressure Signatures and Loudness Carpets

Marian Nemec* and Michael J. Aftosmis†
NASA Ames Research Center, Moffett Field, CA 94035, USA
Liam Smith‡
Georgia Tech School of Aerospace Engineering, Atlanta, GA 30332, USA

A non-intrusive uncertainty quantification method is applied to computational analysis of supersonic, low-boom aircraft. The mean and standard deviation statistics of the pressure waveforms and loudness metrics are evaluated through use of numerical quadrature. The probability density function (p.d.f.) of these outputs is evaluated via kernel density estimation. The simulations use an inviscid, embedded-boundary Cartesian-mesh flow solver in the nearfield combined with an augmented Burgers' equation solver for propagation in the farfield. The results show that the p.d.f. of the waveform is bimodal at shocks, which makes the mean and standard deviation statistics inappropriate. Despite this limitation, we show that the moment statistics can provide effective assessment of discrepancies when comparing with experimental data. This is demonstrated by presenting uncertainty analysis of a wind-tunnel test and showing that we significantly improve the predictions when we include the test uncertainties in the simulation. Normal distributions are obtained for the ground signature and loudness metrics, which is primarily due to the careful shaping of the low-boom waveform. Separation of variables and error control are used to reduce computational cost. We demonstrate that this is an efficient approach in the sense of balancing numerical errors in the statistics quadrature with discretization errors in the solvers.

I. Introduction

The key design goal for the new X-59 Quiet SuperSonic Technology X-plane is that the loudness of its sonic-boom does not exceed 75 dB at cruise.[1] This is roughly equivalent to the rumblings of a distant thunderstorm or ambient city noise. Simulation-based analysis using Computational Fluid Dynamics has played a major role in designing for this low-boom requirement. The simulations, together with wind-tunnel tests, show that the loudness requirement can be satisfied at on-design conditions. A major challenge in reliably predicting boom loudness, however, are off-design conditions. This is because the problem is dominated by shocks and complex flowfields that are sensitive to many uncertainties, including perturbations in operating conditions, aircraft configuration and the state of the atmosphere.[2–7]

Estimation of statistics via numerical quadrature has been shown to work well for problems with discontinuities.[8–10] In particular, an uncertainty propagation framework has been developed by Barth[11–13] that features specialized quadrature techniques for non-smooth data. The framework is non-intrusive, i.e., the estimation of statistics reduces to a set of independent, deterministic simulations. Reliable estimates of expectation (mean) and variance have been demonstrated for various aerodynamic outputs, including lift, drag and pressure distributions. In addition to the moment statistics, the framework provides estimates of the probability density function (p.d.f.) to fully characterize uncertainty in the predictions.

The objective of this work is to evaluate the framework proposed by Barth[11–13] for uncertainty analysis in low-boom problems. We start by assessing the effect of uncertainties on the predicted nearfield pressure signature. This is a pressure waveform extracted from the flowfield near the aircraft that is dominated by

*Aerospace Engineer, Computational Aerosciences Branch, MS 258-5; marian.nemec@nasa.gov, Senior Member AIAA.
†Aerospace Engineer, Computational Aerosciences Branch; michael.aftosmis@nasa.gov, Associate Fellow AIAA.
‡Graduate Research Assistant, Lsmith98@gatech.edu, AIAA Student Member.

shocks and propagated to the ground. We examine the p.d.f. of the signature to determine if the mean and standard deviation are the appropriate statistics for this output. While the goal of low-boom uncertainty analysis is capturing uncertainty in noise levels on the ground, characterizing uncertainties in the nearfield is critical for validating nearfield solvers. This is because the predictions are compared to wind-tunnel measurements. We examine if including uncertainties observed in wind-tunnel tests as part of the simulation can help explain experimental discrepancies, since measuring low-boom signatures is no easy task.[14–17]

To characterize low-boom noise on the ground, we track six scalar outputs involving four loudness metrics, the shock travel-time and the loudness-carpet width, i.e., the extent of noise on the ground perpendicular to the flight path. The loudness metrics derive directly from the ground pressure signature. For low noise, the pressure signatures are shaped to avoid formation of N-waves and, therefore, are less likely to contain discontinuities once propagated to the ground. We investigate the implications of shaped signatures on the moment statics of loudness metrics and the carpet width.

Additional objectives are to investigate strategies for reducing computational cost and to improve the integration of low-boom uncertainty quantification into the aircraft design process. A new feature of the framework[11–13] is the evaluation and tracking of numerical errors in the statistics and the p.d.f. We leverage this capability to explore an error balancing approach to minimize the number of simulations required to characterize the output uncertainty.

II. Problem Formulation and Governing Equations

We use a well established simulation approach for sonic-boom prediction.[2,18] The problem domain is divided into nearfield and farfield regions, as illustrated in Fig.1. In the nearfield, we solve the steady, three-dimensional Euler equations governing compressible flow of a perfect gas to determine the nearfield pressure signature. For a finite region of space with volume V and surface area A, the integral form of the Euler equations is given by

$$\frac{\mathrm{d}}{\mathrm{d}t}\int_V \mathbf{Q}\,\mathrm{d}V + \oint_A \mathbf{F}\cdot\hat{\mathbf{n}}\,\mathrm{d}A = \mathbf{0} \tag{1}$$

where $\mathbf{Q} = [\rho, \rho\mathbf{U}, \rho E]^{\mathrm{T}} = [\rho, \rho u, \rho v, \rho w, \rho E]^{\mathrm{T}}$ are the non-dimensional conserved variables, and

$$\mathbf{F}\cdot\hat{\mathbf{n}} = \begin{bmatrix} \rho U_{\mathrm{n}} \\ \rho U_{\mathrm{n}}\mathbf{U} + p\hat{\mathbf{n}} \\ (\rho E + p)U_{\mathrm{n}} \end{bmatrix} \tag{2}$$

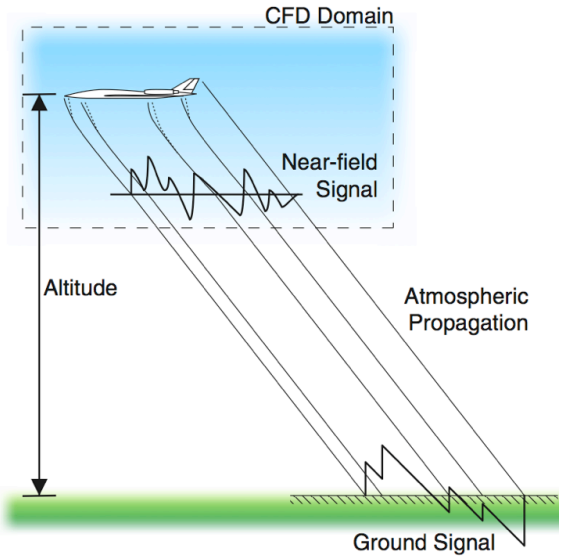


Figure 1: Sonic-boom domain decomposition

where $U_{\mathrm{n}} = \mathbf{U}\cdot\hat{\mathbf{n}}$ and $\hat{\mathbf{n}}$ is the outward facing unit normal. In the farfield, the evolution of the nearfield waveform as it descends through a stratified and windy atmosphere to the ground is modeled using the augmented Burgers' equation[19–21]

$$\frac{\partial p}{\partial \sigma} = p\frac{\partial p}{\partial \tau} + \frac{1}{\Gamma}\frac{\partial^2 p}{\partial \tau^2} + \sum_{\nu} C_\nu \left(1 + \theta_\nu \frac{\partial}{\partial \tau}\right)^{-1} \frac{\partial^2 p}{\partial \tau^2} - \frac{p}{2S}\frac{\partial S}{\partial \sigma} + \frac{p}{\rho_0 c_0}\frac{\partial(\rho_0 c_0)}{\partial \sigma} \tag{3}$$

where p is pressure, σ the distance, τ the retarded time, C_ν the dispersion parameter, Γ the thermoviscous parameter, θ_ν the molecular-relaxation time parameter of the ν^{th} relaxation process, ρ_0 and c_0 the local density and speed of sound, respectively, and S the ray tube area of adjacent ray paths.

The primary output quantities of interest, J, are the nearfield and ground pressure signatures, and the loudness metrics derived from the ground signature, such as perceived loudness (PLdB) and various weightings of the sound exposure levels (A/B/C/D-SEL dB). These are not only evaluated directly under the flight path (on-track), as indicated in Fig.1, but also off-track, i.e., in the lateral direction, to determine the full sonic-boom carpet.[2]

To characterize uncertainty in J, we seek to determine the expectation (mean) and variance (square of standard deviation) moment statistics. Let ξ denote an input random variable of the simulation, e.g., uncertainty in freestream Mach number, angle of attack, or altitude, that is distributed by a probability density function $f(\xi)$. The expectation is given by

$$E[J(p(x,\xi))] = \int J(p(x,\xi))f(\xi)d\xi \tag{4}$$

where we emphasize the dependence of the functional J on the pressure signature $p(x,\xi)$ and note that J may be a scalar, e.g., a loudness metric, or a vector. The variance and standard deviation are given by

$$V[J] = \sigma^2[J] = \int (J - E[J])^2 f(\xi)d\xi \tag{5}$$

Furthermore, we seek to fully characterize the uncertainty in J by estimating its probability density function

$$\text{Prob}[a \leq J \leq b] = \int_a^b p(\xi)d\xi \tag{6}$$

While determining p may not be necessary in every case, we use the p.d.f. to validate the moment statistics due to the presence of shock discontinuities in the pressure signature.

III. Numerical Methods

A. Nearfield and Farfield Solvers

Equation 1 is discretized on a multilevel Cartesian mesh with embedded boundaries. The mesh consists of regular Cartesian hexahedra everywhere, except for a layer of body-intersecting cells, or cut cells, adjacent to the wetted surface of the geometry, as illustrated in Fig. 2. The spatial discretization uses a cell-centered, second-order accurate finite volume method, resulting in a system of equations

$$\mathbf{R}_H(\mathbf{Q}_H) = 0 \tag{7}$$

evaluated on a mesh with an average cell size H, which we call the *working* mesh. The vector $\mathbf{Q}_H = [\bar{Q}_1, \bar{Q}_2, \ldots, \bar{Q}_N]^{\mathrm{T}}$ is the discrete solution vector of the cell-averaged values for all N cells of the mesh. The flux-vector splitting approach of van Leer[22] is used. Steady-state flow solutions are obtained using a five-stage Runge–Kutta scheme with local time-stepping, multigrid, and a domain decomposition scheme for parallel computing.[23–25] We use the van Leer limiter and 4-level multigrid in this work. All boundary conditions are enforced weakly.[26,27] In the farfield, we use the sBOOM atmospheric shock propagation solver developed by Rallabhandi[20,28] to propagate a waveform extracted from the nearfield and to compute loudness metrics. Equation 3 is solved in the time domain using operator splitting and a finite-difference discretization along ray paths that account for the state of the atmosphere. Both solvers have been thoroughly validated for use in sonic-boom prediction.[29–32]

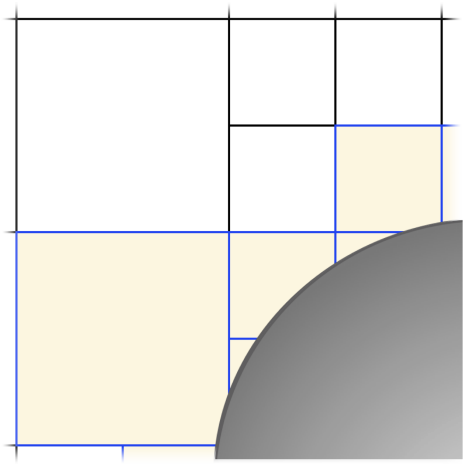


Figure 2: Multilevel Cartesian mesh in two-dimensions with a cut-cell boundary. Adjacent cells cannot exceed 2:1 ratio.

B. Statistics

Uncertainty estimates are obtained via the QUEST-Lite uncertainty quantification software developed by Barth.[11–13] Equations 4 and 5 are evaluated through use of numerical quadrature, where the integrals are converted to a summation over N realizations of the output (simulations) corresponding to N quadrature values of the random variable ξ

$$J_H(p_H(x,\xi_1)),\ J_H(p_H(x,\xi_2)),\ \ldots,\ J_H(p_H(x,\xi_N)) \tag{8}$$

resulting in a discrete form of Eq. 4 given by

$$E_N[J_H] = \sum_{i=1}^{N} (w\, J_H)_i \tag{9}$$

where w is an algebraic vector of quadrature weights. For example, if ξ is the freestream Mach number, then statistics for the loudness metrics due to variability in the input Mach number are determined from N independent flow simulations. The expression for variance is similar. This approach is nonintrusive since no modifications of the nearfield or farfield solvers are required to compute the statistics. In this work, we use the multi-level, node-nested Clenshaw-Curtis dense quadrature. For a single random variable, $N = 2^{L-1} + 1$ for quadrature levels $L \geq 2$. Typical values of L range from three to six.

Note that the pressure signature contains many sharp discontinuities due to shocks propagating from the aircraft. This makes the integrands in Eqs. 4 and 5 non-smooth and adversely impacts the accuracy of numerical quadratures. To improve accuracy when discontinuities are present, we use the HYGAP algorithm proposed by Barth[11] for dense quadratures. This algorithm checks for smoothness and adaptively constructs a piecewise, non-oscillatory polynomial approximation of the output when discontinuities are detected.

Kernel density estimation is used to estimate the probability density function p in Eq. 6. The approach is described by Barth[10,12,13] and is based on a Gaussian kernel. The approach reuses the HYGAP algorithm to construct a response surface for J to allow draws from a large population of samples ($\gg N$) efficiently. This is required especially when p is multi-modal.

C. Numerical Error Estimates and Error Control

The finite discretization, i.e., characteristic cell-size H, used in the nearfield and farfield solvers, the choice of the timestep during the farfield propagation, and the number of nodes, N, used to evaluate the statistics quadrature all contribute to numerical errors that affect the accuracy of the statistics. Consider the numerical error in the evaluation of the expected value

$$\varepsilon = E[J] - E_N[J_H] \tag{10}$$

where $E[J]$ is the exact expectation of the output functional with no numerical error given by Eq. 4. The second term $E_N[J_H]$ is given by Eq. 9 and contains both the statistics quadrature and solver discretization errors. To estimate ε, we follow the work of Barth[11,13] and assume that the discretization error is known

$$\varepsilon_H = J - J_H \tag{11}$$

for each realization required by the N-point quadrature. Next, let ε_Q represent the numerical error in the statistics quadrature

$$\varepsilon_Q[J_H] = E[J_H] - E_N[J_H] \tag{12}$$

for the discrete output J_H. The linearity property of the expectation is used to rewrite Eq. 10 as

$$\begin{aligned} \varepsilon &= E[J] - E[J_H] + E[J_H] - E_N[J_H] && (13)\\ &= E[\varepsilon_H] + \varepsilon_Q[J_H] && (14) \end{aligned}$$

where the first term $E[\varepsilon_H]$ represents the error in the expectation (mean) due to discretization error of the Cart3D and sBOOM solvers and the second term is the statistics quadrature error described above.

Equation 14 provides a useful decomposition of the expectation error estimate. The main idea is to balance the two error contributions, while driving ε below a specified tolerance. On one hand, if the quadrature error is dominant, $\varepsilon_Q \gg E[\varepsilon_H]$, then the quadrature level L should be increased and computational resources should be dedicated to obtaining more realizations for the statistics. Alternatively, J_H could be evaluated on coarser meshes and with larger timesteps, resulting in faster turn-around. On the other hand, if the solver discretization error is dominant, $E[\varepsilon_H] \gg \varepsilon_Q$, then computational resources should be dedicated to solving on finer meshes and with smaller timesteps. Alternatively, cost savings could be realized by evaluating the statistics using coarser quadratures.

The evaluation of $E[\varepsilon_H]$ may seem problematic since it involves the exact expectation. However, it can be expanded into two computable terms

$$E[\varepsilon_H] = E_N[\varepsilon_H] + \varepsilon_Q[\varepsilon_H] \tag{15}$$

Barth[11,13] further refines Eqs. 14 and 15 to distinguish cases when only error magnitudes are provided, and derives error representation formulas and error bounds for variance and standard deviation. Furthermore, a procedure for correcting the output probability density distribution for discretization errors is also provided.

1. *Nearfield and Farfield Discretization Error*

Prediction of ε via Eq. 10 hinges on the accuracy of the discretization error estimate ε_H in Eq. 11. For the three-dimensional nearfield simulation, we use the method of adjoint weighted residuals in conjunction adaptive mesh refinement to estimate and control discretization errors. Since the farfield simulation is lower-dimensional, we use uniform refinement in space and time to make sure that the discretization error in the farfield simulation does not dominate. We provide a brief overview, starting with the mesh adaptation in the nearfield. To estimate the discretization error ε_H, we consider isotropic refinement of the working mesh to obtain an embedded mesh with average cell size h containing approximately eight times the numbers of cells (in three dimensions). The goal is to affordably estimate the error relative to the embedded mesh

$$e = J_h - J_H \tag{16}$$

and then rely on asymptotic analysis[33] to determine the total discretization error

$$\varepsilon_H = \left(1 + \frac{1}{r^p - 1}\right) e \tag{17}$$

where p is the order of accuracy of the spatial discretization and r is the refinement ratio, H/h. For example, for a first-order scheme, $p = 1$, and uniform refinement, $r = 2$, Eq. 17 reduces to $\varepsilon_H = 2e$.

Our approach to estimate J_h is based on the work of Venditti and Darmofal.[34] The details of the implementation are given in Ref. 27, 35, where the expression for the output on the embedded mesh is given by

$$J_h \approx J_h(\mathbf{Q}_\mathrm{L}) - \underbrace{(\boldsymbol{\psi}_h^H)^\mathrm{T}\,\mathbf{R}_h(\mathbf{Q}_\mathrm{L})}_{\text{Adjoint Correction}} - \underbrace{(\boldsymbol{\psi}_h - \boldsymbol{\psi}_h^H)^\mathrm{T}\,\mathbf{R}_h(\mathbf{Q}_\mathrm{L})}_{\text{Remaining Error}} \tag{18}$$

with $\mathbf{Q}_\mathrm{L} = \mathbf{P}_\mathrm{L}\mathbf{Q}_H$, where $\mathbf{P}_\mathrm{L}$ represents a linear prolongation operator, and $\boldsymbol{\psi}_h^H$ denotes a reconstruction of adjoint variables from the working mesh to the embedded mesh. We approximate $\boldsymbol{\psi}_h$ in Eq. 18 with a triquadratic interpolant, $\boldsymbol{\psi}_\mathrm{TQ}$, and $\boldsymbol{\psi}_h^H$ with a trilinear interpolant, $\boldsymbol{\psi}_\mathrm{TL}$. The adjoint variables satisfy the following linear system of equations on the working mesh

$$\left[\frac{\partial \mathbf{R}_H(\mathbf{Q}_H)}{\partial \mathbf{Q}_H}\right]^\mathrm{T} \boldsymbol{\psi}_H = \frac{\partial J_H(\mathbf{Q}_H)}{\partial \mathbf{Q}_H}^\mathrm{T} \tag{19}$$

To obtain a computable error estimate, we split Eq. 18 into an estimate for the corrected functional

$$J_c = J_h(\mathbf{Q}_\mathrm{L}) - \boldsymbol{\psi}_\mathrm{TQ}^\mathrm{T}\,\mathbf{R}_h(\mathbf{Q}_\mathrm{L}) \tag{20}$$

and a cell-wise estimate of the remaining error in each cell of the working mesh

$$\boldsymbol{\eta}_H = \sum_{j \in \mathrm{V}_i} \left(\boldsymbol{\psi}_\mathrm{TQ} - \boldsymbol{\psi}_\mathrm{TL}\right)^\mathrm{T} \mathbf{R}_h(\mathbf{Q}_\mathrm{L})_j \tag{21}$$

where j denotes the j^th child of parent cell V_i and $\boldsymbol{\eta}_H = [\eta_1, \eta_2, \ldots, \eta_N]^\mathrm{T}$. Substituting Eq. 20 into Eq. 16 gives an estimate of the relative error

$$e \approx J_c - J_H \tag{22}$$

without solving on the embedded mesh. To define a local quantity suitable for driving adaptive mesh refinement, the remaining error, Eq. 21, is localized to form a cell-wise error indicator

$$|\boldsymbol{\eta}|_H = [|\eta_1|, |\eta_2|, \ldots, |\eta_N|]^\mathrm{T} \tag{23}$$

When the output of interest is the nearfield pressure signature, the form of the adaptation functional is given by

$$J_\mathrm{s} = \int_0^L \left(\frac{p(x) - p_\infty}{p_\infty}\right)^2 \mathrm{d}x \tag{24}$$

where L is the length of the sensor line. To obtain a point-wise error distribution for the signature, we use Richardson and Aitken extrapolations from the finest three meshes of the adaptation.[30,36] The procedure calculates an observed order of accuracy for the signature based on the L_1 norm of pressure differences between the mesh levels. The observed order is assumed to be constant and is applied point-wise to estimate local discretization errors. The same procedure is also used to estimate the ground pressure signature error.

2. *Statistics Quadrature Error*

The order of error for the Clenshaw-Curtis quadrature is $\mathcal{O}(N^{-r})$ for a univariate functional with r bounded derivatives. Barth[11] takes advantage of the node-nested property of the quadrature and implements a backward formula using levels L, $L-1$ and $L-2$ to estimate the quadrature error terms $\varepsilon_Q[\cdot]$ in Eqs. 12 and 15. The HYGAP algorithm and additional safeguards are used when the integrands lack sufficient regularity r in the stochastic dimension.

D. Managing Computational Cost

So far, we assumed that ξ represents a single random variable. Practical sonic-boom problems, however, involve many sources of uncertainty. A limitation of dense quadratures is that their computational cost increases exponentially with the number of random variables. This is due to their tensor product form when applied to problems in multiple stochastic dimensions. For example, to characterize the effects of uncertainty due to freestream Mach number and angle of attack using $L = 4$ quadrature requires $N = 9 \times 9 = 81$ simulations. This becomes impractical once the problem involves more than about five random variables, despite the error balancing strategy of Eq.14.

To manage this computational cost, we exploit the hyperbolic nature of sonic-boom simulations. Recall Fig. 1 and Sec. II that outline the problem decomposition into the nearfield and farfield domains. Many parameters associated with the farfield, such as altitude, ground height, winds, atmospheric temperature and humidity distributions, do not affect the inviscid nearfield simulation. Furthermore, propagation is cheaper than a nearfield simulation. This motivates a decomposition of the random variables into two sets: those that affect the nearfield and those that do not. A nearfield database is precomputed for the nearfield random variable set, thereby eliminating duplicate work. For example, expand the example above to include uncertainty in flight altitude, in addition to the Mach number and angle of attack. For the $L = 4$ quadrature, a naive implementation requires $N = 9 \times 9 \times 9 = 729$ simulations, but of those only 81 are unique nearfield simulations. Hence, it is advantageous to precompute the 81 unique nearfields and simply reuse them when propagating from different altitudes to complete all the realizations required by the quadrature. Additional, problem-specific cost saving strategies are discussed in the Results section.

IV. Results

To thoroughly evaluate uncertainty propagation in low-boom analysis, the results are presented in three parts. We begin with uncertainty in the nearfield domain and focus on the nearfield signature. The middle section considers uncertainties associated with atmospheric propagation, with focus on the ground signature and loudness metrics. We end with the fully-coupled problem and characterize uncertainty in the loudness carpet. Nearfield simulations are performed using Cart3D version 1.5.7. For farfield simulations, sBOOM version 2.86-3 is used. For uncertainty quantification, QUEST-Lite version 3 is used with HYGAP postprocessing.

A. Nearfield Signature Uncertainty

1. *NACA 0012 Airfoil with Freestream Uncertainty*

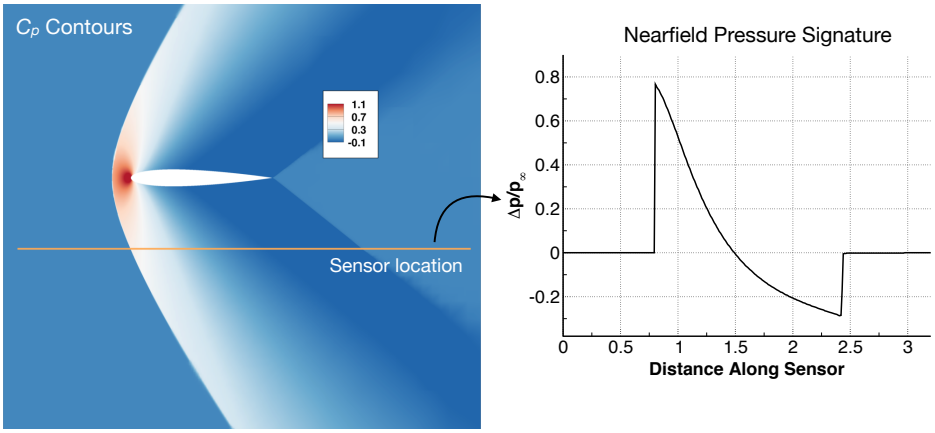
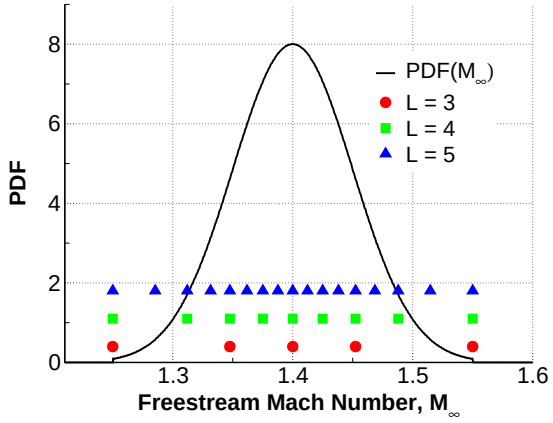
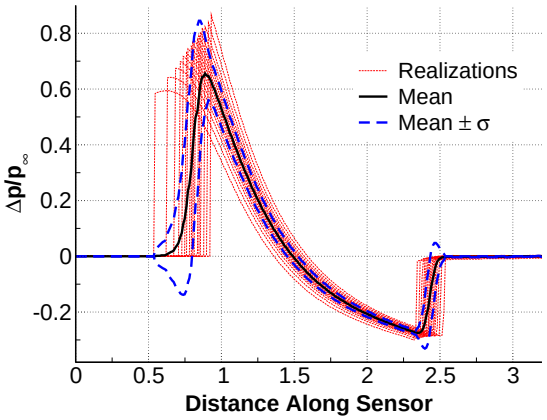


Figure 3: Near-body flow (left) and pressure signature (right) for the NACA 0012 airfoil at $M_\infty = 1.4$

We begin with an idealized problem to demonstrate statistics estimation and error control in shock-dominated problems that involve uncertainty characterization of the nearfield pressure signature. Consider a flow simulation for the NACA 0012 airfoil of unit chord at freestream conditions $M_\infty = 1.4$ and $\alpha = 0°$. A pressure signature is extracted half-a-chord below the airfoil along a sensor of length 3.2 chords. The domain boundary is 64 chords away. Figure 3 shows the airfoil, the near-body flow, the location of the pressure sensor and the pressure signature. The signature is dominated by the leading- and trailing-edge shocks linked by a smooth expansion.



(a) Input uncertainty M_∞ = Gaussian$_{3\sigma}$(mean = $1.4, \sigma = 0.05$) and nodes for quadrature levels L



(b) Nearfield pressure signatures and statistics due to normally distributed freestream Mach number

Figure 4: Characterization of the input random variable M_∞ (left) and the resulting statistics for the output pressure signature (right) for the NACA 0012 airfoil

We assume that the freestream Mach number is uncertain: M_∞ = Gaussian$_{3\sigma}$(mean = $1.4, \sigma = 0.05$). Figure 4a shows the distribution (black line), which is truncated at three standard deviations and normalized to have unit total probability. How does this uncertainty affect the nearfield signature? To answer this question, we choose $L = 5$ quadrature and evaluate the statistics. Recall from Sec. III.B that a 5-level quadrature implies $N = 17$ realizations to estimate the mean via Eq. 9 and the standard deviation. Figure 4a shows the location of the quadrature nodes (blue triangles), as well as nodes for lower levels, $L = 3$ (red circles) and $L = 4$ (green squares), to illustrate the nesting property of the Clenshaw-Curtis quadrature. Note that all levels include the mean and the 3σ endpoints[a].

[a]The points are plotted with a constant vertical offset for clarity. Only the location with respect to the x-axis is meaningful.

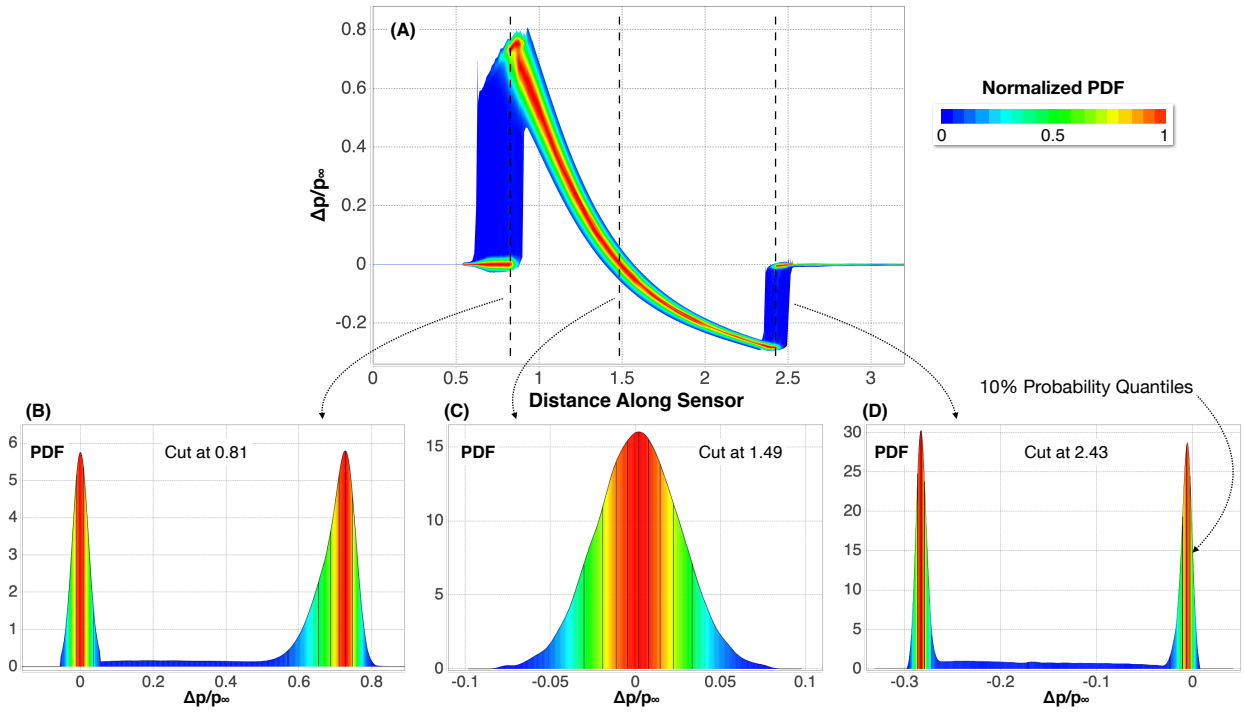
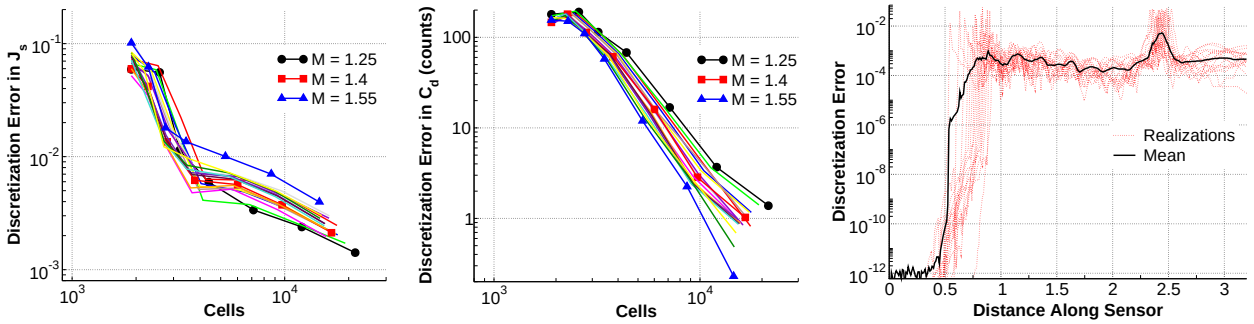


Figure 5: (A) Probability density function p for the nearfield signature due to uncertain Mach number. (B) p cut in the front-shock region showing a bimodal distribution. (C) p cut near the zero-crossing of the expansion showing a normal distribution. (D) p cut in the aft-shock region showing a bimodal distribution. Vertical lines in frames B, C and D mark 10% quantiles.

Figure 4b shows all 17 realizations of the pressure signature (red lines), an estimate of the mean (black line) and the standard deviation envelope (dashed line). Realizations with the weakest shocks, i.e., smallest pressure jumps, correspond to the low Mach numbers of the input distribution. To examine the statistics, we start with the expansion region of the signature in the interval $[0.9, 2.3]$ in Fig. 4b. In this region, the moment statistics (mean and standard deviation) characterize the signature uncertainty well. In the interval $[0.5, 0.9]$ containing the front shock, however, the characterization of uncertainty is not satisfactory. We observe that the mean poorly captures the shock discontinuity and the peak overpressures. The mean takes on values between the freestream and peak overpressures that blur out the shock region. The standard deviation performs even worse. It indicates an expansion in the interval $[0.5, 0.8]$, which is not supported by any of the realizations. Similar observations apply in the recompression interval $[2.3, 2.6]$, except the aft shock is weaker so the smearing of the mean and the standard deviation overshoots are less pronounced.

To understand the poor performance of the moment statistics, we compute the probability density function p from the 17 realizations. Figure 5 shows the p.d.f. of the whole signature in Frame A, while Frames B, C and D show cross-cuts at various locations along the signature normalized to have unit total probability. p fully characterizes the uncertainty and intuitively captures the variations observed in the realizations. In the interval $[0.6, 0.9]$ that contains the front shock, p is bimodal (Frame B) and correctly indicates high probability of both the freestream and peak-overpressure states. Once in the expansion region, the distribution quickly becomes Gaussian (Frame C). Similar to the front-shock region, a bimodal distribution is observed in the aft-shock region (Frame D). When p is approximately Gaussian, the moment statistics perform well, as expected. When the distribution is bimodal, the moment statistics are inappropriate — the mean overpressure ends up in a low-probability region between the peaks and the standard deviation roughly correlates with the distance between the peaks, which mischaracterizes the spread of the data as observed in Fig. 4b. Similar bimodal distributions were also observed by Barth[13] for transonic flow cases.

Having characterized the signature uncertainty, we now examine bias due to numerical error. We begin with discretization error in the realizations. The simulations use Eq. 24 to guide the mesh refinement and minimize discretization error in the pressure signature. The initial mesh is uniform near the airfoil with cell-size $H \approx 12\%$ of chord and seven adaptations are performed to obtain the final mesh. The cell adaptation



(a) ε_H in J_s (b) ε_H in C_d (c) ε_H for pressure signatures and $E[\varepsilon_H]$

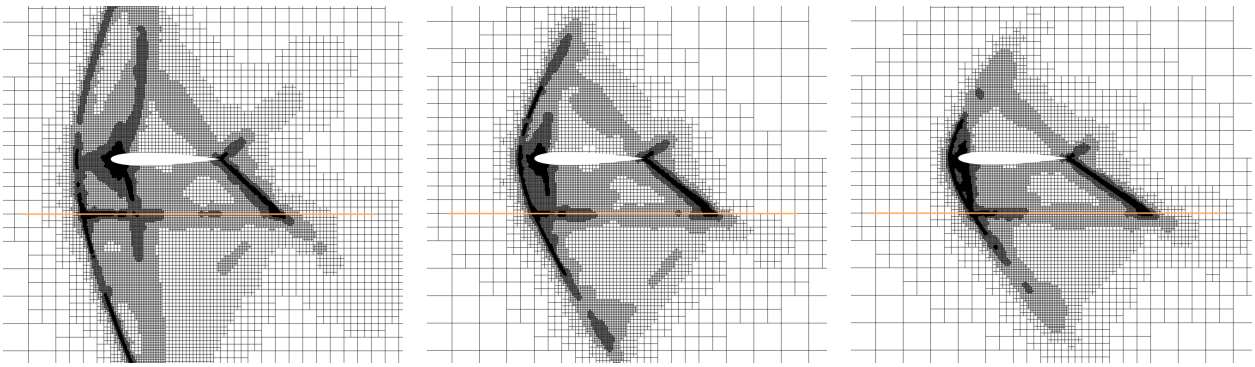
Figure 6: Estimate of discretization error ε_H, Eq. 11, for all 17 realizations. Mean and 3σ simulations are indicated with symbols in (a) and (b) that also mark adaptation cycles.

threshold is set to the mean error indicator value of Eq. 23. Figure 6a shows the history of the discretization error estimate ε_H, Eq. 11, for J_s up to the penultimate mesh[b]. The error is reduced almost 100 fold in all 17 simulations. We also monitor error in the drag coefficient, C_d, to provide a more intuitive assessment of the error level. Figure 6b shows that on the penultimate mesh the discretization error in C_d is approximately one count in all simulations.

Figure 6c shows the point-wise error distribution for all realizations of the pressure signature (red lines). These error estimates are obtained via the asymptotic error analysis described in Sec. III.C.1 using signatures from the last three meshes of the adaptation. Figure 7 shows examples of the final meshes near the airfoil for the mean and 3σ values of M_∞ with the location of the pressure sensor indicated (orange line). We observe in Figs. 6 and 7 that as M_∞ increases, the number of cells decreases. This trend is due to the shrinking zone of dependence of the pressure signature as M_∞ increases, because the refinement pattern is primarily confined by the front bow shock that becomes more oblique with increasing M_∞. As expected, the errors in the realizations (red lines in Fig. 6c) are highest through the two shock regions in intervals $[0.5, 0.9]$ and $[2.3, 2.6]$. These error distributions are used to estimate the level of discretization error in the mean, $E[\varepsilon_H]$ via Eq. 15, shown as black line in Fig. 6c. Given the non-smoothness of the pressure signature and the bimodal regions of the p.d.f., the mean error tracks the realizations fairly well, especially through the expansion and the second shock.

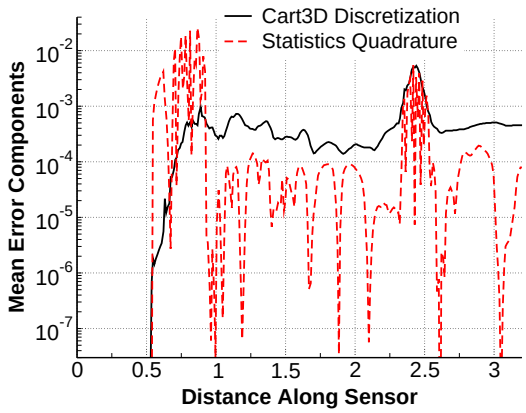
Figure 8a shows the numerical error balance for the estimate of the mean, ε in Eq. 14. The black line is Cart3D discretization error $E[\varepsilon_H]$, replotted from Fig. 6c. The red line is the numerical error due to the $L = 5$ quadrature, i.e., $\varepsilon_Q[J_H]$ in Eq. 12 obtained as described in Sec. III.C.2. The two error contributions are well balanced through the expansion region in the interval $[0.9, 2.3]$. The discretization error is about half-an-order-of-magnitude larger, suggesting that a coarser quadrature, e.g., $L = 4$, could be used to obtain

[b]The mesh adaptation algorithm does not usually evaluate error on the final mesh to maximize efficiency[35]

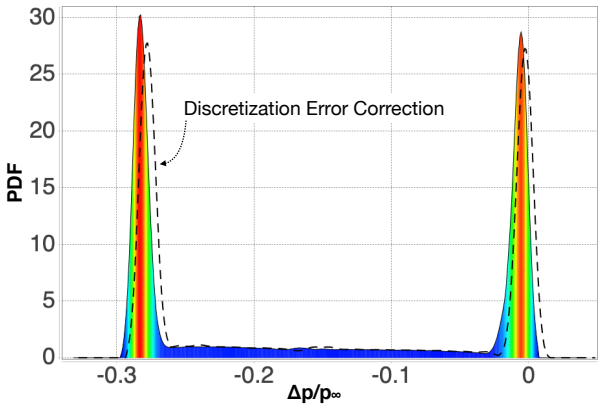


(a) $M_\infty = 1.25$, 46,925 cells (b) $M_\infty = 1.4$, 33,672 cells (c) $M_\infty = 1.55$, 28,945 cells

Figure 7: Near-body meshes for the mean and 3σ realizations of M_∞ with the location of the sensor indicated



(a) Numerical error balance: realization $E[\varepsilon_H]$ and quadrature $\varepsilon_Q[J_H]$ errors



(b) Corrected p for discretization error

Figure 8: Numerical error balance for the mean (left) and p.d.f of aft-shock region with discretization error correction (right)

similar results. In the shock regions, upstream and downstream of the expansion, the error estimates are less reliable due to the non-smoothness of the integrands in the statistics and the bimodal nature of the p.d.f. A practical way to assess the level of error in these regions is to recompute p with the realization errors, i.e., those shown in Fig. 6c, included as a corrrection. Figure 8b shows the original, bimodal p, reproduced from Fig. 5(d), and the corrected p (dashed line) for discretization error in the aft-shock region of the signature. The correction is relatively small, confirming that the level of discretization error in the realizations is small, and the slight shift to the right is expected since the post-shock pressure (right peak) should approach freestream as the discretization error vanishes. Note that the inclusion of realization errors shifts the p.d.f. by a constant offset without significantly changing the spread of the data. This systematic bias was also observed by Barth[13] in transonic and subsonic flow cases, noting a shift in the mean and no change in standard deviation.

2. LM 1044 Low-Boom Model

Validation of nearfield solvers is an important application of uncertainty quantification for nearfield pressure signatures. We present a practical example based on tests in the NASA Ames 9×7 ft. supersonic wind tunnel in 2012.[17] Figure 9 shows a model of the LM 1044 low-boom configuration (upper left), which was one of several configurations tested to generate a high-quality database to validate predictions of nearfield solvers. For this study, we choose a version of the LM 1044 geometry without the under-wing nacelles. We include the blade strut, shown in Fig. 9, that was used in the tests to minimize model support interference. The reference length of the model is 19.027 inches and the nose is positioned 32.6 inches above the sensor ($h_{\text{nose}} = 32.6$ and $R/L = 1.7$).

We focus on the on-track signature and run a simulation at the test conditions $M_\infty = 1.7$ and $\alpha = 2.17°$. The tunnel walls are not included in the simulation. The center panel in Fig. 9 shows Mach number contours on a plane through the model centerline to highlight the propagation of the numerous weak shocks from the model to the sensor (white line). The right panel shows the underlying mesh on the same cutting plane. The colors indicate refinement levels, with smallest cells visible near the model and along the shocks between the model and the sensor. The final mesh contains approximately 60 million cells and is obtained after six cycles of adaptive mesh refinement using Eq. 24 as the output of interest. The pressure signature plot (Fig. 9, lower left) shows the computed (dashed line) and measured (solid line) signatures. While the computed signature matches the morphology of the measured signature, there is significant disagreement in the peak overpressures at the shocks and the discontinuities are significantly sharper in the simulation.

One reason for this mismatch is model-form error, i.e., the assumption of inviscid flow[c]. Viscous effects alone, however, do not seem sufficient to explain the pressure differences observed at the first shock, generated by the nose, and along the pressure ramp in the interval $[0.06, 0.3]$ in Fig. 9. We expect a thin boundary layer

[c]The Reynolds number in the experiment was relatively low, 4.43×10^6 per foot.[17]

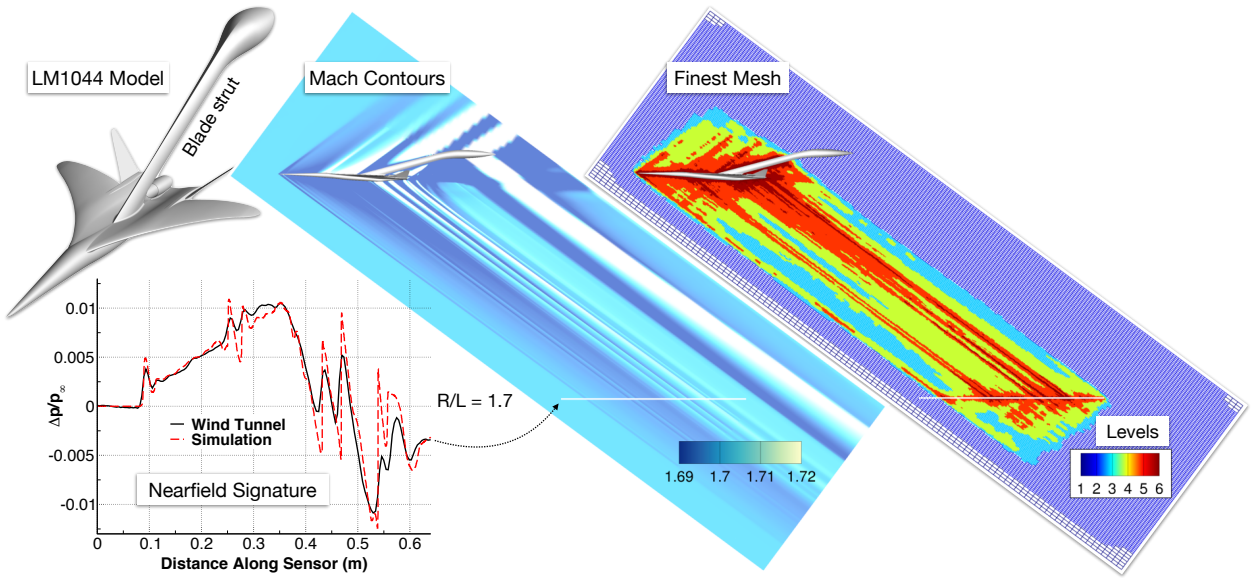


Figure 9: LM 1044 model (upper left), Mach contours on plane of symmetry with pressure sensor indicated (center), final mesh after six adaptations (right), and extracted pressure signature with comparison to measured data (lower left), $M_\infty = 1.7$ and $\alpha = 2.17°$

in this region with negligible influence on the signature. Therefore, we investigate if including uncertainties associated with the test in the simulation improves the agreement between the two signatures.

To reduce the influence of background fluctuations and flow bias in the tunnel,[14–16] the measured signature shown in Fig. 9 (lower left) is actually the arithmetic mean of signatures collected by the RF1 pressure rail[37] at 26 successive positions in the test section.[17] Figure 10 shows the 26 signatures recorded during the test, the mean signature (black line) and the standard deviation (dashed line). There is considerable variation in the signatures at the shocks and the rooftop interval $[0.28, 0.36]$. Furthermore, the 26 signatures are temporal averages at each position based on data collection events with different time exposures. At each collection event, the angle of attack, the sideslip angle and the h_{nose} displacement were recorded in addition to the signature.

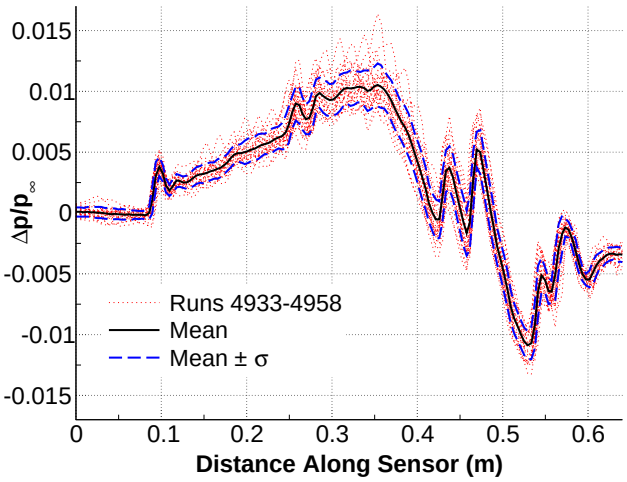


Figure 10: Pressure signatures from each of the 26 model positions for the LM 1044 tests, and the resulting mean signature and standard deviation.

To capture the variability in the model orientation and position during the test, we introduce α and h_{nose} as random variables in the simulation[d]. Rather than assume a probability distribution, we construct the p.d.f. for these variables from the test data. For each of the 26 model positions we assume a normal distribution centered on the temporal mean and and a standard deviation set by the range of the temporal data collected at each model position. These are summed and normalized to obtain a p.d.f. for each variable. Figure 11 shows the probability density functions for α (left) and h_{nose} (right) along with the individual Gaussians used at each model position. We also assume uncertainty in the freestream Mach number to account for flow variability in the test section during the model traversals. Based on previous studies of flow quality in supersonic wind tunnels,[38,39] we choose a uniform distribution with a 1/2-width of 0.005, $M_\infty = \text{Uniform}[1.695, 1.705]$.

[d]We examined variability in the sideslip angle and found that over the range observed in the tests $(0.4 - 0.7°)$ it has negligible impact on the pressure signature. A value of 0.6° is used in all simulations.

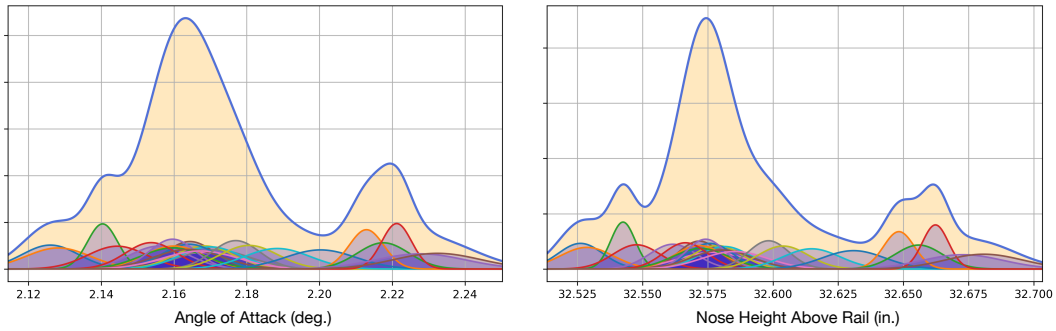
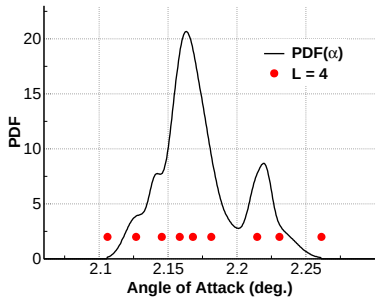
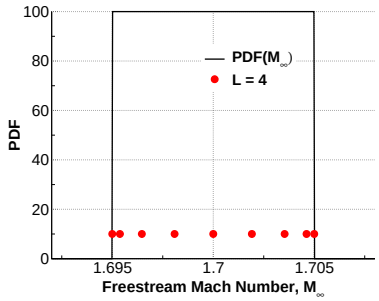


Figure 11: Estimated probability density functions for α (left) and h_{nose} (right) from the LM 1044 tests.

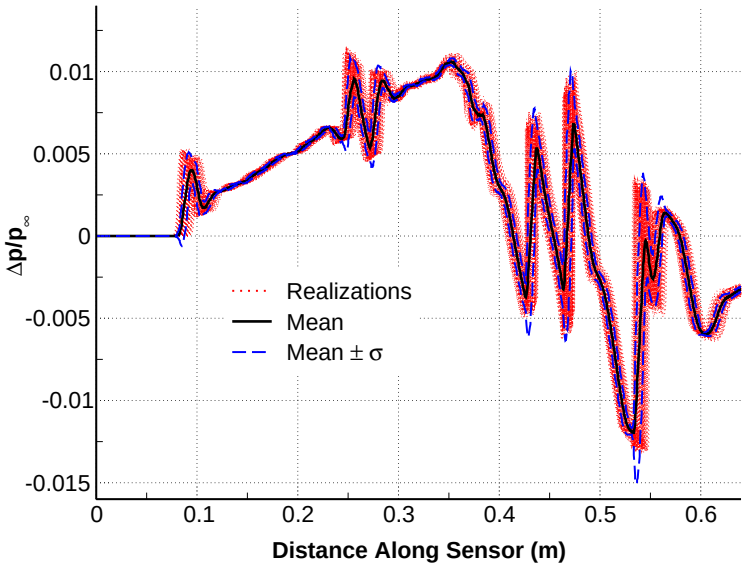
Note that the shape of the two distributions shown in Fig. 11 is quite similar. Closer examination of the test data indicates that the two variables are not independent, i.e., large angles of attack correlate with large h_{nose} distances. The model is essentially oscillating about a rotation center located some distance downstream. Hence, to orient and position the model, we use the α p.d.f. and rotate about a point aft of the body to match the observed h_{nose} heights. This reduces the uncertainty problem to two independent random variables, angle of attack and Mach number. We apply the angle of attack via a rotation of the model because it is more efficient to solve the problem on a Mach aligned mesh (Fig. 9).



(a) Custom p.d.f.



(b) Uniform[1.695,1.705]



(c) Pressure signatures and moment statistics

Figure 12: Input random variables (left), and 81 output realizations and moment statistics for the LM 1044 simulation (right)

We use $L = (4, 4)$ quadrature to estimate the statistics, which implies that $N = 81$ realizations are required to estimate the mean via Eq. 9 and the standard deviation. Figures 12a and 12b show the distributions for the random variables and the $L = 4$ quadrature nodes. Note the adaptive sampling of the custom p.d.f. with nodes automatically distributed to capture the highest probability regions. Figure 12c shows all 81 realizations of the pressure signature (red lines), the mean signature (black line) and the standard deviation envelope (dashed line). Similar to Fig. 4b, the standard deviation over-predicts the spread of the data at the shocks and the mean poorly characterizes the discontinuities. Despite these shortcomings, which are explained in the previous NACA 0012 example, these statistics closely mimic the signature averaging process used in the test. To demonstrate, Fig. 13 compares the obtained mean signature (Simulation with Uncertainty) with the

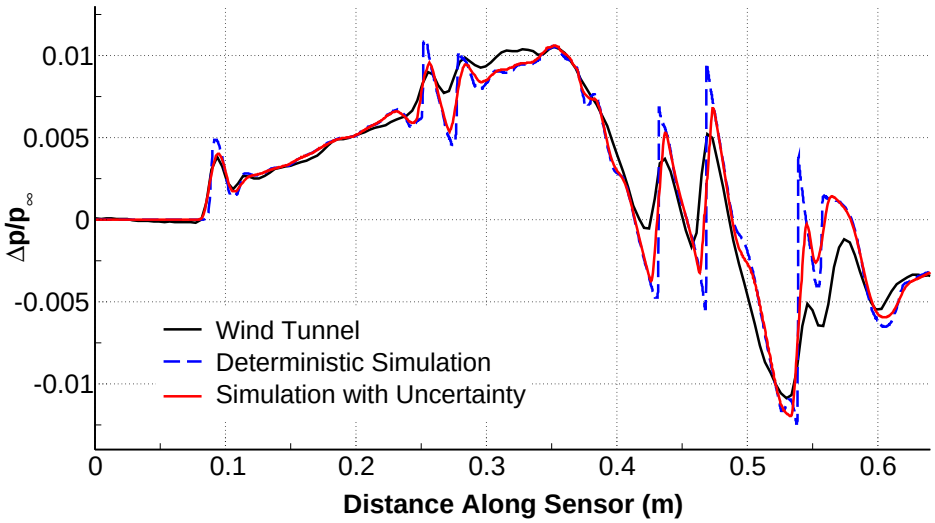
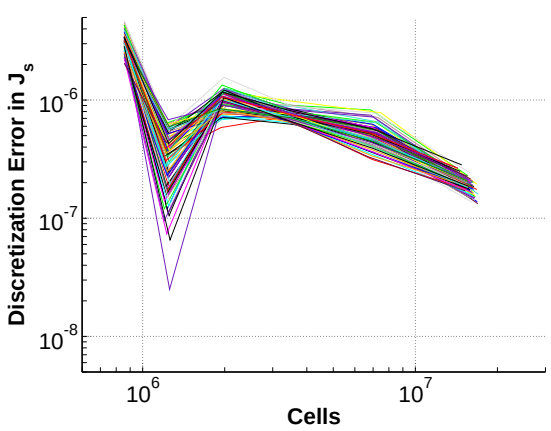
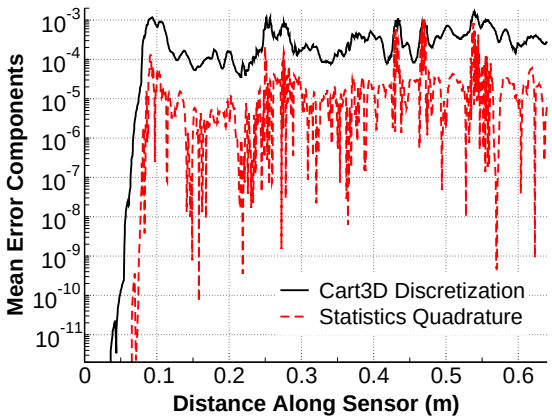


Figure 13: Assessment of experimental discrepancy: pressure signatures obtained from the LM 1044 test (Wind Tunnel), simulation with no statistical uncertainty (Deterministic Simulation) and the mean signature obtained via uncertainty analysis (Simulation with Uncertainty)

measured signature (Wind Tunnel) and the deterministic simulation at the nominal conditions (Deterministic Simulation) that are shown in Fig. 9. The agreement with the measured signature is significantly improved, especially on the forebody where the boundary layer is thin $[0.05, 0.25]$. The agreement in amplitude and period of the first shock is excellent. The uncertainty analysis does not capture the deviation observed in the rooftop interval $[0.29, 0.35]$, but it does reduce the amplitude and crispness of all the shocks in the aft portion of the signature resulting in a much better comparison with the averaged wind-tunnel data. Moreover, there is good agreement in the shape of the signature in the aft interval $[0.55, 0.6]$, except the simulation is shifted upward by a constant offset. Results in Fig. 13 are an important step toward reliably bounding modeling errors. The results show that uncertainties observed in the experiment need to be included in the simulation to properly gage the observed experimental discrepancy.



(a) ε_H adaptation history, 81 realizations



(b) Numerical error balance: realization $E[\varepsilon_H]$ and quadrature $\varepsilon_Q[J_H]$ errors

Figure 14: Convergence of error estimate for all realizations (left) and numerical error balance for the mean signature of the LM 1044 simulation (right)

To check the pollution of the mean signature due to numerical errors ε, we evaluate the error terms in Eq. 14. Figure 14a shows the mesh adaptation convergence history of the discretization error in J_s (Eq. 24) for all realizations. The discretization error is reduced by more than an order of magnitude in every case. We use this to verify that the mesh is sufficiently refined before computing the point-wise discretization error

of the mean signature. Figure 14b shows the resulting error balance between the mean discretization error $E[\varepsilon_H]$ (black line) and the numerical error due to the $L = (4, 4)$ quadrature $\varepsilon_Q[J_H]$ (red line). Surprisingly, the quadrature errors are approximately a factor of ten smaller than the mean discretization error, except in the areas of the aft shocks. This suggests that to reduce the overall numerical error, a finer mesh is needed to reduce the level of discretization error, despite the relatively coarse numerical quadrature.

B. Uncertainty in the Farfield

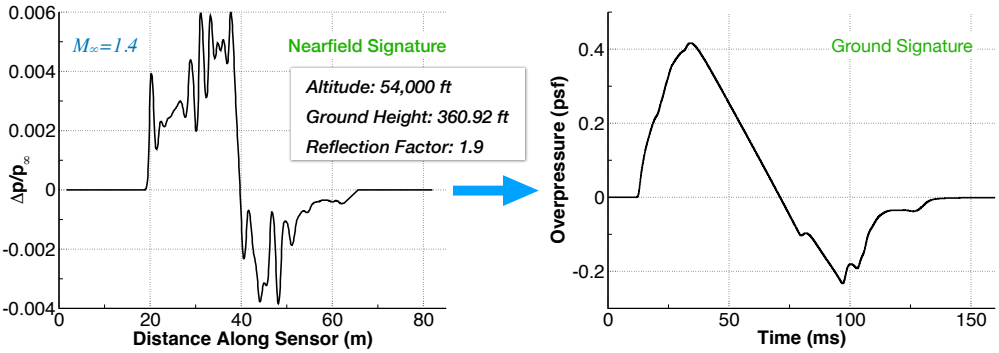
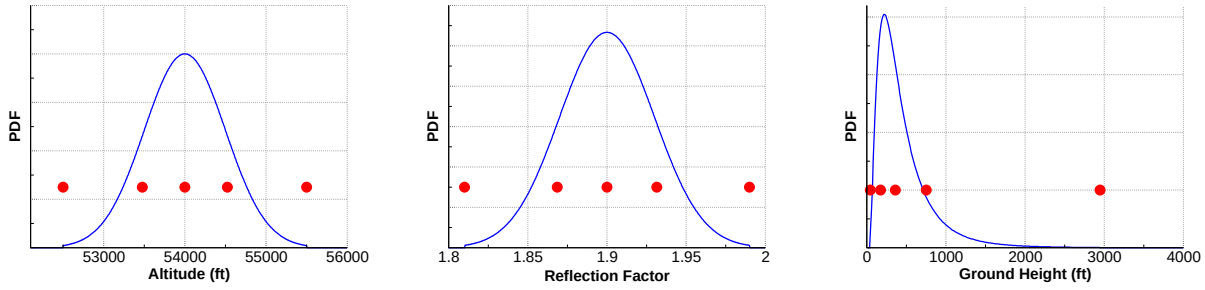


Figure 15: Case 2 from SBPW3: Nearfield signature (left), and Ground signature (right)

In this section, we isolate the farfield simulation to characterize uncertainty in the prediction of sonic-boom loudness without the compounding influence of uncertainty from the nearfield. In other words, in contrast to Sec. A, the freestream Mach number and nearfield pressure signature are assumed to have no statistical variation. We use propagation Case 2 from the Third AIAA Sonic Boom Propagation Workshop (SBPW3).[31,32] Figure 15 summarizes the case, showing the nearfield signature from the workshop and the propagated ground signature. We consider only the on-track case and use a sampling frequency of 150 kHz to propagate all signatures.

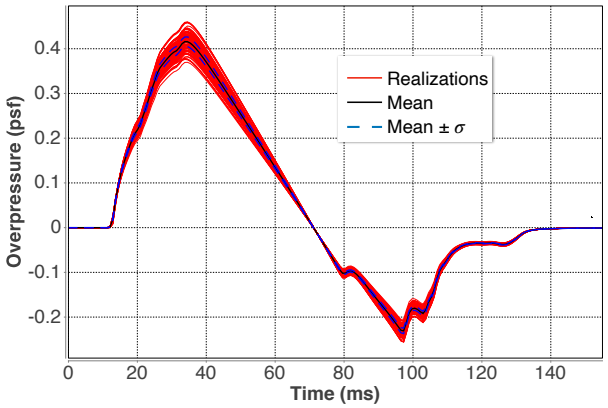


(a) $\text{Normal}_{3\sigma}(m = 54k, \sigma = 0.5k)$ (b) $\text{Normal}_{3\sigma}(m = 1.9, \sigma = 0.03)$ (c) $\text{LogNormal}_{3\sigma}(m = 360.92, \sigma = 0.7)$

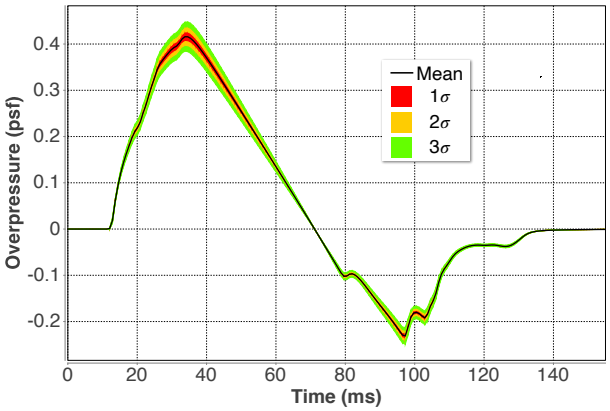
Figure 16: Input variable uncertainties (m denotes mean). The red symbols are $L = 3$ quadrature points.

We assume uncertainty in three inputs: flight altitude, ground height and ground reflection factor. Figure 15 shows their nominal values. Altitude and reflection factor are assumed to be normally distributed, and a log-normal distribution is used for ground height, as shown in Fig. 16. The distributions are truncated at three standard deviations and normalized to have unit total probability. The standard deviation for the reflection factor accounts for flight over water, where it is likely to be closer to 2, and flight over densely wooded areas, where the reflection factor is likely to be below its nominal value of 1.9. For ground height, the log-normal distribution captures terrain variations between coastal areas and mountainous regions, with coastal areas being much more likely since more people live there. To evaluate the statistics, we choose $L = (3, 3, 3)$ quadrature, which has five evaluation points per random variable for a total of $N = 5 \times 5 \times 5 = 125$ realizations. The quadrature points are shown as red circles in Fig. 16.

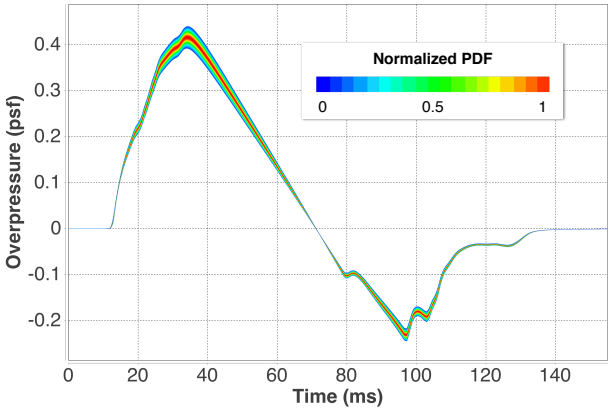
We begin by examining the statistics of the ground pressure signature. Figure 17a shows all 125 realizations of the signature, as well as the mean signature and the standard deviation envelope. There are



(a) Realizations, $E_N[J_H]$ and $\sigma_N[J_H]$



(b) 3σ plot



(c) p.d.f.

Figure 17: Uncertainty quantification for on-track ground signature

no spurious, or anomalous, signatures in the dataset. The input uncertainty has no influence on the zero crossing and period of the signature, and primarily affects amplitude and rise-time. Figure 17b shows the 3σ spread of the data. In contrast to Fig. 4b, the moment statistics reliably characterize the uncertainty. This is explained by examining the probability density function p of the signature. Figure 17c shows that overpressure is normally distributed over the whole duration and is therefore reliably characterized by the moment statistics. This is despite the presence of shocks in the nearfield signature shown in Fig. 15. The dissipative processes of the propagation, including relaxation losses, appear to be dominating the non-linear effects and result in smooth variations of the signature in the stochastic dimensions for the three input variables. It is likely that this observation is limited to shaped ground signatures. For example, a p.d.f. for N-waves should be bimodal, similar to Fig. 5, especially if the input random variables affect the period.

Next, we examine the statistics of noise metrics. Figure 18 shows all realizations in the random variable space with each realization colored by the level of perceived loudness (PLdB). Maximum loudness occurs for cases with a high reflection factor and ground height, e.g. Lake Tahoe, in combination with the lowest flight

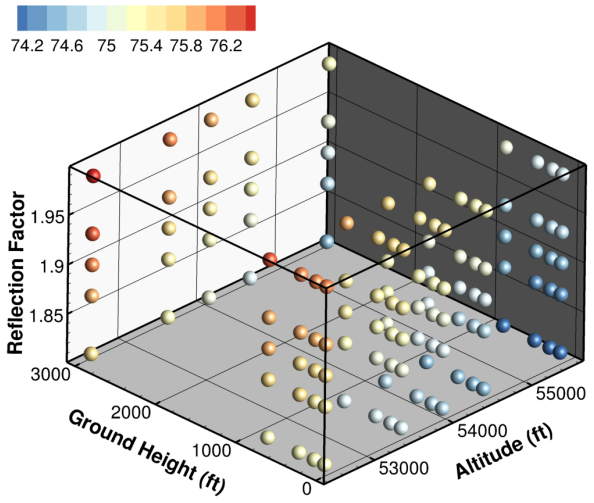
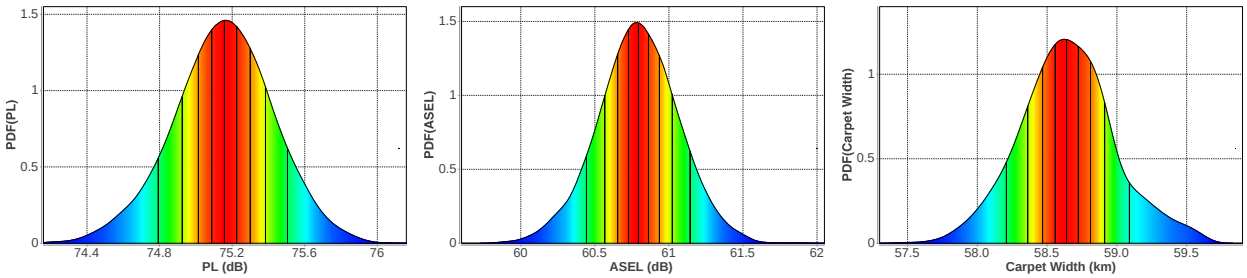


Figure 18: All realizations (125) colored by level of perceived loudness (PLdB)



(a) Preceived Loudness (b) A-Weighted Sound Exposure Level (c) Sonic-Boom Capet Width

Figure 19: Probability density functions for noise metrics and boom carpet width. Black vertical lines mark 10% quantiles and colors represent normalized probability: red=1 (very likely) and blue=0.01 (unlikely).

altitude. Conversely, quietest cases involve a low reflection factor and ground height, e.g. coastal redwood forests, and highest flight altitude. The scatter plot indicates that there are no anomalous noise estimates. Similar plots are obtained for the other loudness metrics.

Figure 19 shows the computed probability density functions for the perceived loudness and A-SEL metrics, and the boom carpet width. The distributions are close to Gaussian with well defined means and standard deviations. Figure 19a shows that the mean for PL is approximately 75.2 dB and the standard deviation is close to 0.3 dB. Hence, the input uncertainty has a moderate impact on ground loudness, especially if the maximum loudness goal is set at 75 dB. Figure 19c shows that a near normal distribution is also obtained for the boom carpet width, with a mean of 58.6 km and standard deviation of 0.4 km. The normal distributions of these outputs are not surprising considering that the ground overpressure is normally distributed and the noise metrics are sums of filtered representations of the signature. Moreover, they simplify the characterization of uncertainty in these problems since the moment statistics are sufficient.

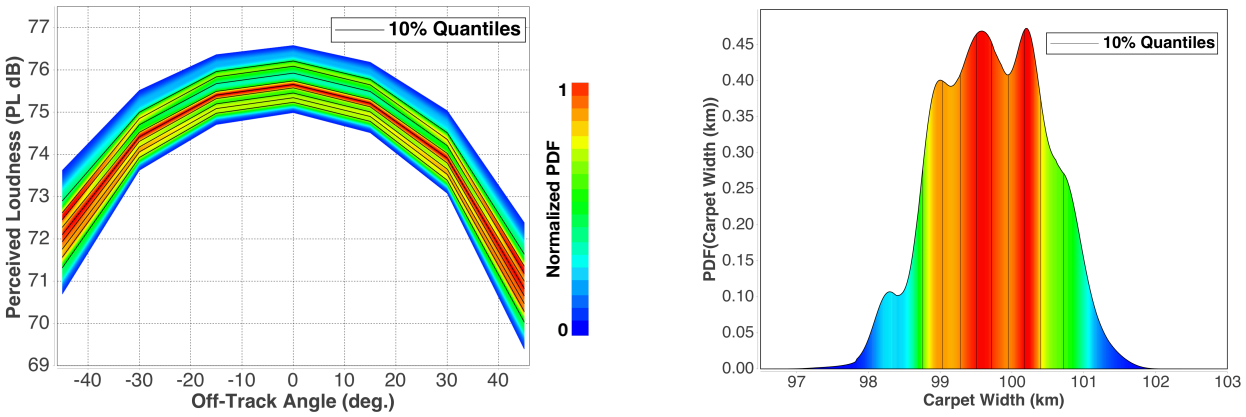
C. Combined Nearfield and Farfield Uncertainty

The final example considers the fully coupled problem involving propagation of input uncertainty through the combined nearfield-farfield simulation. Our goal is to demonstrate further applications of computing probability density functions for graph outputs. In all previous examples, the output of interest is the pressure signature, but the problem formulation is not limited to this output. In this example, we consider the p.d.f. of the loudness carpet and the carpet width. We use Case 1 from the propagation section of the Second AIAA Sonic Boom Propagation Workshop.[30,40] The case involves flow over an axisymmetric body and propagation through a windy atmosphere from an altitude of about 16km. We choose freestream Mach number as a random variable: $M_\infty = \text{Gaussian}_{3\sigma}(\text{mean} = 1.6, \sigma = 0.02)$.

Figure 20 shows the probability density functions associated with the two outputs. Figure 20a shows uncertainty in the loudness carpet, where "Off-Track Angle" denotes the cross-range angle between the aircraft and the ground. An off-track angle of zero degrees corresponds to being directly below the flight path, or on-track. No sonic-booms reach the ground past the cutoff angle, which in this case is close to 45° and slightly asymmetric due to wind. The results show that the loudness p.d.f. deviates from Gaussian only near the edges. The variation is about 0.5 dB over most of the carpet. Figure 20b shows the p.d.f. for the boom carpet width. The distribution is multimodal, showing that most likely values are 99.5 and 100.3 km.

V. Conclusions

An uncertainty quantification toolkit has been evaluated in the context of shock-dominated flows relevant to low-boom aircraft analysis. To assess the effect of uncertainties on predicted outputs, numerical quadrature is used to estimate the mean and standard deviation statistics and the same quadrature points are also used to estimate the output p.d.f. via discrete kernel convolution. The outputs of interest are pressure signatures, loudness metrics and the ground loudness carpet (sonic-boom footprint). The input random variables involve the freestream conditions, such as Mach number, angle of attack and altitude, and additional parameters related to atmospheric propagation. Most inputs are assumed to be uniformly or normally distributed, but we also test a custom distribution based on observed data.



(a) Sonic-boom loudness carpet

(b) Sonic-boom capet width

Figure 20: Probability density functions for loudness carpet and carpet width due to uncertainty in M_∞.

We obtained reliable statistics for all test cases despite the presence of shocks that lead to discontinuities in the stochastic dimensions. In particular, uncertainty analysis of the nearfield signature highlights the importance of computing the p.d.f., because the distribution is bimodal at the shocks. This means that the moment statistics can be misleading near the shocks. We observed standard deviation values outside the range of the data in both nearfield examples. In contrast, the moment statistics are sufficient to characterize uncertainty in the farfield. This is demonstrated for shaped ground signatures and associated loudness metrics. We confirmed that these outputs are normally distributed. Importantly, the results show the usefulness of uncertainty analysis for correctly interpreting discrepancy between wind-tunnel tests and simulations. We demonstrate that it is difficult to gage modeling errors without carefully characterizing uncertainties observed in tests and accounting for signature postprocessing techniques.

Peak computational efficiency is achieved by monitoring the error balance between the level of discretization error in the realizations and the numerical error due to the statistics quadrature. This allows evaluation of the total numerical error in the predicted statistics and also helps guide resource allocation to address the largest error, either by increasing the quadrature level or further refining the computational mesh. Additional computational savings are realized by isolating the random variables that affect the nearfield and precomputing all unique nearfield simulations, thereby minimizing the dimensionality of the nearfield run matrix. In the future, we plan to evaluate sparse quadratures and assess error converge rates to further improve turn-around for larger problems.

Acknowledgements

The authors gratefully acknowledge support from the NASA ARMD Commercial Supersonic Technology Project. Resources supporting this work were provided by the NASA High-End Computing (HEC) Program through the NASA Advanced Supercomputing (NAS) Division at Ames Research Center. The authors thank Tim Barth (NASA Ames) for his assistance with QUEST and for helpful discussions; Don Durston (NASA Ames) for providing tunnel data, and candid discussions of test techniques and tunnel uncertainty; Jeff Housman (NASA Ames) for helpful discussions on flow non-uniformity in the 9×7 supersonic tunnel; and Wade Spurlock (Science & Technology Corp.) for help with LM 1044 case setup.

References

[1] "Low-Boom Flight Demonstration," https://www.nasa.gov/X59, Accessed: 2021-5-26.

[2] Maglieri, D. J., Bobbitt, P. J., Plotkin, K. J., Shepherd, K. P., Coen, P. G., and Richwine, D. M., "Sonic Boom: Six Decades of Research," NASA/SP-2014-622, 2014, http://hdl.handle.net/2060/20150006843.

[3] Alonso, J. J. and Colonno, M. R., "Multidisciplinary Optimization with Applications to Sonic-Boom Minimization," *Annu. Rev. Fluid Mech.*, Vol. 44, 2012, pp. 505–526. doi:10.1146/annurev-fluid-120710-101133.

[4] West, T. K., Reuter, B. W., Walker, E. L., Kleb, B., and Park, M. A., "Uncertainty Quantification and Certification Prediction of Low-Boom Supersonic Aircraft Configurations," *Journal of Aircraft*, Vol. 54, No. 1, 2017, pp. 40–53.

doi:10.2514/1.C033907, https://doi.org/10.2514/1.C033907.

[5]Rallabhandi, S. K., West, T. K., and Nielsen, E. J., "Uncertainty Analysis and Robust Design of Low-Boom Concepts Using Atmospheric Adjoints," *Journal of Aircraft*, Vol. 54, No. 3, 2017, pp. 902–917. doi:10.2514/1.C033908.

[6]Phillips, B. D. and West, T. K., "Trim Flight Conditions for a Low-Boom Aircraft Design Under Uncertainty," *Journal of Aircraft*, Vol. 56, No. 1, 2019, pp. 53–67. doi:10.2514/1.C034932.

[7]Phillips, B. D., Heath, C., and Schmidt, J., "System-Level Impact of Propulsive Uncertainties for Low-Boom Aircraft Concepts," AIAA Paper 2020-2730, June 2020. doi:10.2514/6.2020-2730, AIAA AVIATION 2020 Forum.

[8]Bijl, H., Lucor, D., Mishra, S., and Schwab, C., editors, *Uncertainty Quantification in Computational Fluid Dynamics*, Vol. 92 of *Lecture Notes in Computational Science and Engineering*. Springer International Publishing, 2013.

[9]Abgrall, R. and Mishra, S., "Uncertainty quantification for hyperbolic systems of conservation laws," Research Report 2016-58, ETH, Dec. 2016, Seminar For Applied Mathematics.

[10]Barth, T. and Sukys, J., "On the Calculation of Exact Cumulative Distribution Statistics for Burgers Equation," NASA TP-2018–220040, National Aeronautics and Space Administration, Center for AeroSpace Information, 7115 Standard Drive, Hanover, MD 21076, 2018, https://ntrs.nasa.gov/citations/20190029285.

[11]Barth, T., "Non-intrusive Uncertainty Propagation with Error Bounds for Conservation Laws Containing Discontinuities," *Uncertainty Quantification in Computational Fluid Dynamics*, edited by H. Bijl, D. Lucor, S. Mishra, and C. Schwab, Springer, 2013.

[12]Barth, T., "An Overview of Combined Uncertainty and A-Posteriori Error Bound Estimates for CFD Calculations," AIAA Paper 2016-1062, Jan. 2016. doi:10.2514/6.2016-1062, 54th AIAA Aerospace Sciences Meeting.

[13]Barth, T., "On the Calculation of Uncertainty Statistics with Error Bounds for CFD Calculations Containing Random Parameters and Fields," *Simulation Credibility: Advances in Verification, Validation, and Uncertainty Quantification*, edited by U. B. Mehta, D. R. Eklund, V. J. Romero, J. A. Pearce, and N. S. Keim, NASA TP—2016–219422 and JANNAF GL—2016–0001, 2016, pp. 211–248, https://www.nas.nasa.gov/assets/pdf/papers/NASA-TP-2016-219422_and_JANNAF-GL-2016-0001.pdf.

[14]Reed, T. D., Pope, T. C., and Cooksey, J. M., "Calibration of Transonic and Supersonic Wind Tunnels," NASA CR-2920, National Aeronautics and Space Administration, Center for AeroSpace Information, 7115 Standard Drive, Hanover, MD 21076, 1977, https://https://ntrs.nasa.gov/citations/19780007115.

[15]Durston, D., Cliff, S., Wayman, T., Merret, J., Elmiligui, A., and Bangert, L., "Near Field Sonic Boom Test on Two Low-Boom Configurations Using Multiple Measurement Techniques at NASA Ames (Invited)," AIAA 2011-3333. doi:10.2514/6.2011-3333, 29th AIAA Applied Aerodynamics Conference.

[16]Morgenstern, J., "How to Accurately Measure Low Sonic Boom or Model Surface Pressure in Supersonic Wind Tunnels," AIAA 2012-3215, 2012. doi:10.2514/6.2012-3215, 30th AIAA Applied Aerodynamics Conference.

[17]Cliff, S. E., Durston, D. A., Elmiligui, A. A., Walker, E. L., and Carter, M. B., "Experimental and Computational Sonic Boom Assessment of Lockheed-Martin N+2 Low Boom Models," NASA/TP 2015-218483, NASA, January 2015.

[18]Page, J. A. and Plotkin, K. J., "An Efficient Method for Incorporating Computational Fluid Dynamics Into Sonic Boom Prediction," *9th AIAA Applied Aerodynamics Conference, AIAA Paper 91–3275*, Baltimore, MD, Sept. 1991.

[19]Cleveland, R. O., *Propagation of Sonic Booms Through a Real, Stratified Atmosphere*, Ph.D. thesis, The University of Texas at Austin, 1995.

[20]Rallabhandi, S. K., "Advanced Sonic Boom Prediction Using the Augmented Burgers Equation," *J. Aircraft*, Vol. 48, No. 4, 2011, pp. 1245–1253. doi:10.2514/1.C031248.

[21]Yamamoto, M., Hashimoto, A., Aoyama, T., and Sakai, T., "A unified approach to an augmented Burgers equation for the propagation of sonic booms," *J. Acoust. Soc. Am.*, Vol. 137, No. 4, 2015, pp. 1857–1866. doi:10.1121/1.4916833.

[22]van Leer, B., "Flux-Vector Splitting for the Euler Equations," ICASE Report 82-30, Sept. 1982.

[23]Aftosmis, M. J., Berger, M. J., and Adomavicius, G., "A Parallel Multilevel Method for Adaptively Refined Cartesian Grids with Embedded Boundaries," AIAA Paper 2000–0808, Reno, NV, Jan. 2000.

[24]Aftosmis, M. J., Berger, M. J., and Murman, S. M., "Applications of Space-Filling-Curves to Cartesian Methods for CFD," AIAA Paper 2004–1232, Reno, NV, Jan. 2004.

[25]Berger, M. J., Aftosmis, M. J., and Murman, S. M., "Analysis of Slope Limiters on Irregular Grids," AIAA Paper 2005–0490, Reno, NV, Jan. 2005.

[26]Rodriguez, D. L., Aftosmis, M. J., and Nemec, M., "Formulation and Implementation of Inflow/Outflow Boundary Conditions to Simulate Propulsive Effects," AIAA Paper 2018-0334, Kissimmee, FL, Jan. 2018. doi:10.2514/6.2018-0334, AIAA SciTech Forum.

[27]Nemec, M., Rodriguez, D. L., and Aftosmis, M. J., "Adjoint-Based Mesh Adaptation and Shape Optimization for Simulations with Propulsion," AIAA 2019-3488, 2019. doi:10.2514/6.2019-3488, AIAA Aviation 2019 Forum.

[28]Rallabhandi, S. K., Nielsen, E. J., and Diskin, B., "Sonic-Boom Mitigation Through Aircraft Design and Adjoint Methodology," *Journal of Aircraft*, Vol. 51, No. 2, 2014, pp. 502–510. doi:10.2514/1.C032189.

[29]Wintzer, M., Nemec, M., and Aftosmis, M. J., "Adjoint-Based Adaptive Mesh Refinement for Sonic Boom Prediction," *26th AIAA Applied Aerodynamics Conference*, No. 2008-6593, AIAA, Honolulu, HI, August 2008.

[30]Anderson, G. R., Aftosmis, M. J., and Nemec, M., "Cart3D Simulations for the Second AIAA Sonic Boom Prediction Workshop," *Journal of Aircraft*, Vol. 56, No. 3, 2019, pp. 896–911. doi:10.2514/1.C034842.

[31]Spurlock, W., Aftosmis, M., and Nemec, M., "Cartesian Mesh Simulations for the Third AIAA Sonic Boom Prediction Workshop," *Journal of Aircraft*, 2021, Accepted for publication.

[32]"3rd AIAA Sonic Boom Prediction Workshop," https://lbpw.larc.nasa.gov/sbpw3, Accessed: 2020-11-12.

[33]Roache, P. J., "Verification of Codes and Calculations," *AIAA Journal*, Vol. 36, No. 5, May 1998, pp. 696–702.

[34]Venditti, D. A. and Darmofal, D. L., "Grid Adaptation for Functional Outputs: Application to Two-Dimensional Inviscid Flow," *Journal of Computational Physics*, Vol. 176, 2002, pp. 40–69. doi:10.1006/jcph.2001.6967.

[35]Nemec, M. and Aftosmis, M. J., "Toward Automatic Verification of Goal-Oriented Flow Simulations," NASA/TM 2014-218386, National Aeronautics and Space Administration, Center for AeroSpace Information, 7115 Standard Drive, Hanover, MD 21076, 2014, http://hdl.handle.net/2060/20150000864.

[36]Park, M. A. and Nemec, M., "Nearfield Summary and Statistical Analysis of the Second AIAA Sonic Boom Prediction Workshop," *Journal of Aircraft*, Vol. 56, No. 3, 2019, pp. 851–875. doi:10.2514/1.C034866.

[37]Cliff, S. E., Elmiligui, A. A., Aftosmis, M. J., Thomas, S. D., Morgenstern, J. M., and Durston, D. A., "Design and Evaluation of a Pressure Rail for Sonic Boom Measurement in Wind Tunnels," *Seventh International Conference on Computational Fluid Dynamics (ICCFD7)*, Paper ICCFD7-2006, Big Island, Hawaii, June 2012.

[38]Elmiligui, A., Cliff, S., Aftosmis, M., Nemec, M., Parlette, E., Wilcox, F., and Bangert, L., "Sonic Boom Computations for a Mach 1.6 Cruise Low Boom Configuration and Comparisons with Wind Tunnel Data (Invited)," AIAA 2011-3496, 2011. doi:10.2514/6.2011-3496, 29th AIAA Applied Aerodynamics Conference.

[39]Housman, J., Akaydin, D., Moini-Yekta, S., and Kiris, C., "Preliminary Simulations of the Ames 9ft x 7ft Supersonic Wind Tunnel," Internal Report, Unpublished, 2014.

[40]Rallabhandi, S. K. and Loubeau, A., "Summary of Propagation Cases of the Second AIAA Sonic Boom Prediction Workshop," *Journal of Aircraft*, Vol. 56, No. 3, 2019, pp. 876–895. doi:10.2514/1.C034805.